Microseismic Detection in Borehole DAS as a Spatial Localization Problem: Cross-System Validation at the 2024 Utah FORGE Stimulation

Isao Kurosawa
e-Technology Innovation Center, ENEOS Xplora Inc., Tokyo 106-0041, Japan
E-mail: kurosawa.isao@eneos.com
ORCID: 0009-0004-7393-8400

This manuscript is a non-peer-reviewed preprint submitted to EarthArXiv. It has been submitted to Seismological Research Letters for peer review. Subsequent versions of this manuscript may therefore differ from this one; if accepted, the final version will be available via the 'Peer-reviewed Publication DOI' link on this page.

Microseismic Detection in Borehole DAS as a Spatial Localization Problem: Cross-System Validation at the 2024 Utah FORGE Stimulation

Isao Kurosawa*

e-Technology Innovation Center, ENEOS Xplora Inc., Tokyo 106-0041, Japan

Corresponding author: Isao Kurosawa,

E-mail: kurosawa.isao@eneos.com

Abstract

Distributed acoustic sensing (DAS) turns borehole fibers into dense seismic arrays, but converting terabytes of continuous strain-rate data into reliable real-time detections remains a bottleneck for induced-seismicity monitoring. We argue that the limiting question for DAS microseismic monitoring has been posed incorrectly. Existing detectors ask whether an event is present in a record; on a dense fiber that question is nearly trivial, whereas the question that constrains downstream monitoring — where along the array the energy originates — is not. We therefore reframe detection as spatial localization on the array: the continuous record is decomposed into overlapping channel-time regions of interest (ROIs), each carrying thirteen physical attributes, and the wavefront is recovered as the subset of ROIs that are mutually consistent under propagation. Applied to the 1,496-channel Neubrex DAS array in Utah FORGE well 16B(78)-32 during the April 2024 stimulation of well 16A(78)-32, the detector reproduces 90% of an independent reference catalog derived from a separate fiber and interrogator, while processing 12-s tiles 2.9-3.7 times faster than real time on one GPU. Controlled experiments confirm the reframing: every model we test captures presence almost equally well (area under the curve about 0.98), whereas localization improves sharply once neighboring ROIs constrain one another, with node-level average precision rising from 0.735 for independent scoring to 0.957, and holding at 0.957 on average under leave-one-stage-out evaluation across all eight stimulation stages — a generalization gap of essentially zero. The reformulation, not any network, is what the data reward. A coherence-based triage of detections absent from the reference catalog, calibrated against known events, identifies at least 26 uncatalogued microearthquakes (about 5 per hour of active injection) in stage 4 alone, nearly all sharing a common apparent slowness. The detector provides a validated, real-time front end for DAS-

based traffic-light systems and source characterization.

Keywords: distributed acoustic sensing; induced seismicity; microseismic detection; spatial localization; cross-system validation; real-time monitoring; enhanced geothermal systems; Utah FORGE

Introduction

Enhanced geothermal systems (EGS) and geological carbon storage both create induced microseismicity whose timely detection underpins reservoir characterization and operational risk management (Grigoli et al., 2017). Distributed acoustic sensing (DAS) converts an optical fiber into thousands of strain-rate channels and has rapidly become a standard monitoring tool in boreholes (Zhan, 2020; Lellouch and Biondi, 2021; Lindsey and Martin, 2021). The 2024 stimulation campaign at the Utah Frontier Observatory for Research in Geothermal Energy (FORGE; Moore et al., 2019) was monitored by several independent fiber-optic systems, producing one of the densest public DAS datasets for induced seismicity to date.

The volume of these data is itself the obstacle. A single 12-s tile of the Neubrex array in well 16B(78)-32 comprises 1,496 channels at 4 kHz, and the eight stimulation stages span 73 hours of triggered acquisition, several terabytes in total. The way this problem has been posed, however, has not kept pace with the data. Across both classical and learning-based approaches, DAS microseismic detection is treated as a classification problem — does a trace, a tile, or a record contain an event? Phase pickers transferred from seismometers (Zhu and Beroza, 2019; Mousavi et al., 2020; Zhu et al., 2023), convolutional and residual detectors trained on labeled fiber data (Stork et al., 2020; Boitz and Shapiro, 2024; Yu et al., 2024), and training-free coherence detectors (Porras et al., 2024) all return, in essence, a present-or-absent decision. On a dense borehole fiber this decision is easy: the same wavefront is written across hundreds of adjacent channels, so even a few physical attributes detect its presence almost perfectly. What that decision does not deliver is the quantity monitoring actually needs — which part of the array the energy came from, the spatial information that anchors location, association, and any subsequent source characterization. We show below that this second question is the hard one, and that it has been obscured by evaluation protocols that report only presence.

We therefore reframe DAS microseismic detection as a spatial localization problem on the array. The continuous record is decomposed into overlapping channel-time regions of interest (ROIs), each summarized by thirteen physical attributes; the wavefront is then recovered as the subset of ROIs whose attributes are mutually consistent under seismic propagation, rather than as a single record-level label. Casting the task this way changes what a detector must do: instead of thresholding one global score it must decide, for every ROI, whether that piece of the array participates in a coherent arrival — a judgment that can be made only by letting neighboring ROIs constrain one another. Enforcing that mutual constraint is a relational computation, and message passing over the ROI graph is simply its natural instrument (van den Ende and Ampuero, 2020; Brody et al., 2022); the ablations below show that the decisive ingredient is the reformulation, not the particular network that carries it out. Separating the two questions — whether an event is present, and where on the array it lies — is what exposes the gap that presence-only evaluation conceals: presence is solved by the attributes alone, whereas localization is solved only once propagation consistency is imposed.

Two properties of the FORGE 2024 dataset make the evaluation unusually strong. First, the reference event catalog (see Data and Resources) was constructed from a different sensing system, the FOGMORE fibers interrogated by Silixa units in well 16B and vertical well 78B, so agreement between our detections and the catalog constitutes a cross-system validation rather than a self-consistency check; the same stimulations were additionally characterized by independent surface nodal-geophone monitoring (Niemz et al., 2025) and full moment-tensor analysis (Niemz et al., 2026). Second, the Neubrex acquisition itself was commissioned for completion diagnostics rather than seismology, and to our knowledge no microseismic catalog has previously been derived from it; detections beyond the reference catalog are therefore both possible and scientifically valuable. We quantify and triage those beyond-catalog detections with a coherence statistic calibrated on known events.

Data

During 3-7 April 2024, eight hydraulic-stimulation stages (3R and 4-10) were injected in the deviated well 16A(78)-32 at Utah FORGE. The neighboring well 16B(78)-32 hosts permanently installed fiber (Fig. 1). We use the triggered DAS archive recorded by a Neubrex interrogator on a single-mode fiber in 16B: 12-s tiles of 1,496 channels at about 1-m spacing, sampled at 4 kHz (48,000 samples per channel per tile), available publicly through the Geothermal Data Repository. The eight stages comprise 21,939 tiles (73.1 hr).

The reference catalog is the FOGMORE microseismic catalog for the same campaign (see Data and Resources), derived from Silixa acquisitions on the FOGMORE multimode fiber in 16B and a single-mode fiber in vertical well 78B, with locations constrained by a three-dimensional velocity model. Across all stages and all confidence levels it contains 23,835 events with origin times, locations, uncertainty ellipsoids, confidence indices (CI), signal-to-noise ratios, and moment magnitudes. Crucially, the catalog and our analyzed data share no interrogator, processing chain, or (for 78B) borehole, so the catalog acts as an independent ground truth.

For supervised training we built 800 graphs from 12-s windows: event windows centered on catalog events with CI >= 65 and at least 100 picked channels, projected onto the Neubrex data via GPS-synchronized absolute time, and noise windows drawn from the same stages. Of these graphs, 424 fall inside the eight cataloged stage windows (17-91 per stage) and 376 sample inter-stage and pre-stage noise. Node labels mark ROIs overlapping the cataloged event; because labels are projected from an independent system, weak events on the Neubrex fiber may carry label noise, a limitation we return to in the Discussion.

Method

The localization reformulation is operationalized in three deterministic steps — build regions of interest, attach physical attributes, and enforce propagation consistency across neighbors — none of which depends on a learned component until the last. The implementation used throughout this study is released as MITOS (see Data and Resources). Graph construction follows a fixed physical recipe (Fig. 2). Each tile is band-pass filtered (20-400 Hz) and divided into overlapping ROIs of 64 channels by 0.25 s (channel step 48, time step 0.10 s), about 3,600 ROIs per tile. Each ROI is summarized by thirteen features: maximum, mean, standard deviation, and variance of amplitude; a short-term/long-term average (STA/LTA) detection score; normalized channel and time coordinates; slant-stack semblance and dip score over apparent slownesses of +/-3 ms per channel; the corresponding maximum stacked amplitude and apparent velocity; peak frequency; and a combined heuristic score. Features other than the coordinate and coherence terms are robust-normalized per tile (median absolute deviation), making the graph insensitive to absolute strain-rate amplitude. Nodes are connected to their nearest neighbors along the channel axis (k=1) and time axis (k=3), with edge weights from feature affinity.

The network is a two-layer GATv2 (hidden width 64, four attention heads; Brody et al.,

2022) producing a logit per node. Node-level training uses class-weighted binary cross-entropy against the projected labels; tile-level presence is obtained by max-pooling node logits (multiple-instance learning), so a single architecture serves both tasks. We benchmark against an identical-capacity multilayer perceptron (MLP) applied to nodes independently (no message passing), a graph convolutional network (GCN; Kipf and Welling, 2017), the original GAT (Velickovic et al., 2018), and a classical baseline, the per-ROI slant-stack semblance itself. All learned models are trained for up to 150 epochs with early stopping (patience 20), batch size 32, AdamW (learning rate 1e-3, weight decay 1e-4), under graph-level 5-fold stratified cross-validation with per-fold feature standardization, so no tile contributes to both training and validation.

For continuous scanning, tiles are first screened by a cheap STA/LTA gate that skips quiet tiles; surviving tiles are converted to graphs on the GPU and scored by the trained GATv2. End-to-end processing takes 3.2-4.2 s per 12-s tile on a single NVIDIA A100, that is 2.9-3.7 times faster than real time, which makes single-stream live monitoring feasible. Detections are declared where the presence profile exceeds a threshold (0.5 unless stated) with a minimum separation of 1.0 s, and are associated against the full reference catalog (all 23,835 events at all confidence levels) within a tolerance of +/-1.5 s; the sensitivity of all conclusions to this tolerance is reported below.

Detections that fail to match any catalog event (beyond-catalog candidates) are triaged with a coherence statistic, stack-z: within sliding 32-channel windows and over the same +/-3 ms-per-channel slowness range used in graph construction, envelopes are slowness-aligned, stacked, smoothed over 5 ms, and the robust signal-to-noise ratio (peak minus median, divided by 1.4826 times the median absolute deviation) is maximized over windows and slownesses. On synthetic tests the statistic separates noise (about 7.5) from weak and strong hyperbolic-moveout events (about 14-70). Rather than fixing an arbitrary cut, we calibrate it on a random sample of 60 catalog-matched detections (known true events): the event threshold is their 10th percentile, so by construction 90% of true events pass. Candidates whose best slowness is below 0.5 ms per channel are excluded as zero-moveout artifacts (for example, electrical spikes).

Results

Event presence is easy; localization is not

At the tile level, all learned models are statistically indistinguishable: presence area under the receiver-operating curve is about 0.98 for the MLP, GCN, GAT, and GATv2 alike, and even the classical semblance baseline reaches 0.96. The thirteen physical features are simply strong enough that any reasonable classifier detects whether an event is present. Architectural claims based on presence metrics alone would therefore be empty, and we do not make them.

Localization tells the opposite story (Fig. 3). Node-level average precision (AP) under 5-fold cross-validation is 0.654 +/- 0.017 for semblance and 0.735 +/- 0.007 for the no-graph MLP, then jumps to 0.927 +/- 0.014 for the GCN once message passing is introduced, a gain of 0.19 that dwarfs the fold-to-fold scatter. Attention adds a further increment (GAT 0.950 +/- 0.017) and GATv2 is best on average (0.957 +/- 0.010), although GAT and GATv2 overlap within one standard deviation. The graph, not the attention flavor, is the decisive ingredient: identifying which ROIs constitute the event requires aggregating evidence across neighboring channels and times.

Cross-stage generalization

Stimulation stages differ in injection program, event rate, and noise, so a detector trained on some stages could in principle memorize stage-specific signatures. Leave-one-stage-out

(LOSO) evaluation refutes this (Fig. 4; Table 1): training on seven stages plus noise and testing on the held-out stage yields GATv2 node-AP between 0.927 (stage 10, the smallest test set) and 0.979 (stage 6), mean 0.957 over three random seeds per stage, with seed scatter of at most 0.010. The held-out mean equals the within-fold mean (0.957), that is, the generalization gap is zero at our measurement precision, and the GATv2-MLP margin (mean 0.726 for the MLP) persists in every stage. The localization skill is therefore a property of the wavefield physics encoded in the graph, not of any single stage.

Continuous scanning and the operating point

Scanning 6.13 hr of continuous stage-4 acquisition (1,838 tiles including the inter-stage screen) produced 815 detections at threshold 0.5, of which 735 (90.2%) match the reference catalog within +/-1.5 s. Raising the threshold trades the beyond-catalog rate, which is an upper bound on the false-positive rate, from 13.1 per hour of scanned record (6.13 hr) at threshold 0.5 down to 1.6 per hour at 0.95, while the match fraction rises from 0.90 to 0.96 (Fig. 5). The association tolerance is not doing the work: varying it from 1.0 to 2.0 s moves the match fraction only from 0.865 to 0.934, and 54 beyond-catalog detections survive even the loosest 2.0-s window (Fig. 6), so the beyond-catalog population cannot be explained as timing mismatch.

Beyond-catalog events

The 80 stage-4 beyond-catalog candidates were triaged with the calibrated stack-z statistic (Fig. 7). Their coherence distribution overlaps that of the known true events: 65 of 80 (81%) exceed the event threshold. After additionally excluding zero-moveout candidates, 26 retain genuine moveout, a conservative rate of 5.0 uncatalogued events per hour of active stage-4 injection (26 events over the 5.25-hr stage window, or equivalently 4.2 per scanned hour); the corresponding upper bound from all 65 event-like candidates is 12.4 per hour on the same basis.

Strikingly, 25 of the 26 genuine-moveout survivors share a common best apparent slowness of -1.2 ms per channel (the remaining one at +1.2 ms per channel), consistent with a common source region rather than scattered noise. Figure 8 shows two representative examples; all exhibit clear hyperbolic moveout across hundreds of channels, with the network's node scores concentrated on the event and the detection time marked. The full annotated set is provided as electronic supplement S1. We describe these as coherence-validated candidate microearthquakes: each was additionally inspected visually, but they have not been located, and we make no magnitude claims for them; an amplitude-based proxy magnitude was attempted and rejected because amplitude at the fiber correlates poorly with catalog magnitude ($r = 0.16$) when source-fiber distance is unknown.

Discussion

Cross-system agreement is the strongest external check available for this dataset. Our detector, trained on labels projected from the FOGMORE catalog but operating on a physically distinct acquisition, independently reproduces 90% of that catalog at the default operating point and 96% at a conservative one. The residual systematic offsets between detection times and catalog origin times (typically 1.9-3.7 s among near-matches) are expected from the comparison of an arrival-based detection on one fiber with an origin time located on another system, and motivated the tolerance-sensitivity analysis of Figure 6.

The beyond-catalog population has three possible explanations: events below the reference catalog's detection threshold, events visible to the Neubrex fiber but not retained by the FOGMORE processing chain, and false positives; because association used the full catalog at all confidence levels, the candidates cannot be low-confidence catalog members. The calibrated coherence triage bounds the third: at most 19% of candidates are noise-like, and the 26 genuine-moveout survivors with a nearly uniform apparent slowness behave like a coherent family of small events. Because no microseismic catalog previously existed for the Neubrex acquisition, even the conservative count establishes that the public archive contains substantial uncatalogued seismicity, and the full-campaign scan (21,939 tiles) with the same resumable pipeline is a mechanical extension of this work.

Three limitations deserve emphasis. First, training labels are projected from an independent system; events weak on the Neubrex fiber may be mislabeled, which bounds the achievable node-AP from above and may partly explain the residual gap to unity. Second, beyond-catalog detections are validated by coherence and visual inspection, not by location; cataloging them as earthquakes requires a location step we have deliberately kept out of scope. Third, the magnitude of uncatalogued events is unknown, since amplitude alone proved uninformative without distances; the natural fix, locating the events, is also the natural next step. The detector outputs (presence plus per-ROI localization) are designed as the front end of such a pipeline: combining the 16B array with the vertical 78B fiber would supply the geometric diversity required for location, and waveform-direct source characterization can then proceed without an interim velocity model.

Operationally, the measured throughput (2.9-3.7 times real time on one GPU, with a screening gate that skips quiet intervals) makes the detector deployable in a traffic-light context for EGS or CO_2-storage monitoring, where decisions must follow detections within seconds. Transfer to other installations, including marine cables, primarily requires re-tuning the physically interpretable graph parameters (slowness range, ROI aperture, frequency band) and re-fitting the normalization, rather than wholesale retraining: the small network (about 10^4 parameters per layer) retrains in minutes once a few hundred labeled windows exist.

Conclusions

We have reframed borehole-DAS microseismic detection as a spatial localization problem on the array and evaluated it on the Neubrex 16B acquisition of the 2024 Utah FORGE stimulation against an independent cross-system reference catalog. The reframing is justified empirically: event presence is captured by the physical attributes alone (every model about 0.98), whereas localizing the arrival along the array — the quantity monitoring actually needs — is solved only once neighboring regions of interest are allowed to constrain one another under propagation, with node-level average precision rising from 0.735 for independent scoring to 0.957, and the same 0.957 retained on average when entire stimulation stages are held out. The continuous-scanning pipeline runs 2.9-3.7 times faster than real time, reproduces 90-96% of the reference catalog depending on the operating point, and, after a coherence triage calibrated on known events, reveals at least 26 uncatalogued microearthquakes (5 per hour of active injection) in stage 4 alone, to our knowledge the first microseismic detections derived from this public dataset. The detector is intended as the validated front end of a fully automated DAS monitoring system, with multi-well location and waveform-direct source characterization as the downstream stages.

Data and Resources

The Neubrex triggered DAS data for well 16B(78)-32 (April 2024) are publicly available from the U.S. Department of Energy Geothermal Data Repository (GDR) data lake (bucket gdr-data-lake, prefix FORGE/DAS/april_2024/Neubrex/16b_triggered/v1.0.0). The specific archive used here is the Neubrex triggered-DAS submission of the Utah FORGE 3-2417 project, available at https://gdr.openei.org/submissions/1824 (last accessed June 2026). The FOGMORE microseismic event catalog and three-dimensional velocity model used as the independent reference are distributed through the GDR as the Utah FORGE 3-2417 DAS microseismic event catalog from the April 2024 stimulation (I. Vera Rodriguez, D. Podrasky, C. Maldaner, T. Coleman, Y. Ma, and J. Ajo-Franklin, Rice University), available at https://gdr.openei.org/submissions/1744 (last accessed June 2026). Neither GDR submission had been assigned a digital object identifier at the time of writing. All processing was performed with open-source Python software (PyTorch, PyTorch Geometric, NumPy, SciPy, ObsPy-independent SEG-Y reader). Analysis code and the derived detection lists are released as MITOS at https://github.com/ISAO9/mitos (last accessed July 2026) and archived at Zenodo with a permanent digital object identifier (doi: 10.5281/zenodo.21452269). The electronic supplement contains the full annotated gallery of representative beyond-catalog events (supplement S1).

Declaration of Competing Interests

The author acknowledges that there are no conflicts of interest recorded.

Acknowledgments

The author thanks the Utah FORGE team, the FOGMORE project, and Neubrex Energy Services for making the data and catalogs publicly available.

References

Brody, S., U. Alon, and E. Yahav (2022). How attentive are graph attention networks?, in Proc. of the International Conference on Learning Representations (ICLR).

Grigoli, F., S. Cesca, E. Priolo, A. P. Rinaldi, J. F. Clinton, T. A. Stabile, B. Dost, M. G. Fernandez, S. Wiemer, and T. Dahm (2017). Current challenges in monitoring, discrimination, and management of induced seismicity related to underground industrial activities: A European perspective, Rev. Geophys. 55, 310-340.

Kipf, T. N., and M. Welling (2017). Semi-supervised classification with graph convolutional networks, in Proc. of the International Conference on Learning Representations (ICLR).

Lellouch, A., and B. L. Biondi (2021). Seismic applications of downhole distributed acoustic sensing, Sensors 21, no. 9, 2897.

Lindsey, N. J., and E. R. Martin (2021). Fiber-optic seismology, Annu. Rev. Earth Planet. Sci. 49, 309-336.

Moore, J., et al. (2019). The Utah Frontier Observatory for Research in Geothermal Energy (FORGE): A laboratory for characterizing, creating and sustaining enhanced geothermal systems, in Proc. 44th Workshop on Geothermal Reservoir Engineering, Stanford University, Stanford, California.

Mousavi, S. M., W. L. Ellsworth, W. Zhu, L. Y. Chuang, and G. C. Beroza (2020). Earthquake transformer: An attentive deep-learning model for simultaneous earthquake detection and phase picking, Nat. Commun. 11, 3952.

Niemz, P., K. Pankow, M. P. Isken, K. Whidden, J. McLennan, and J. Moore (2025). Mapping fracture zones with nodal geophone patches: Insights from induced microseismicity during the 2024 stimulations at Utah FORGE, Seismol. Res. Lett. 96, no. 3, 1603-1618, doi: 10.1785/0220240300.

Niemz, P., G. Petersen, J. Rutledge, K. Whidden, and K. Pankow (2026). Isotropic components of microseismic moment tensors at Utah FORGE reveal a diversity of fluid pathway creation processes in EGS development, Sci. Rep. 16, 12916, doi: 10.1038/s41598-026-42493-0.

van den Ende, M. P. A., and J.-P. Ampuero (2020). Automated seismic source characterization using deep graph neural networks, Geophys. Res. Lett. 47, e2020GL088690.

Velickovic, P., G. Cucurull, A. Casanova, A. Romero, P. Lio, and Y. Bengio (2018). Graph attention networks, in Proc. of the International Conference on Learning Representations (ICLR).

Zhan, Z. (2020). Distributed acoustic sensing turns fiber-optic cables into sensitive seismic antennas, Seismol. Res. Lett. 91, 1-15.

Zhu, W., and G. C. Beroza (2019). PhaseNet: A deep-neural-network-based seismic arrival-time picking method, Geophys. J. Int. 216, 261-273.

Table 1. Leave-one-stage-out node-level localization (average precision, mean +/- standard deviation over three random seeds). n is the number of test graphs in the held-out stage.

Held-out stage	**n**	**MLP (no graph)**	**GATv2**
3R	17	0.732 +/- 0.001	0.951 +/- 0.001
4	36	0.689 +/- 0.000	0.958 +/- 0.003
5	62	0.739 +/- 0.001	0.959 +/- 0.010
6	84	0.726 +/- 0.001	0.979 +/- 0.003
7	60	0.727 +/- 0.000	0.973 +/- 0.003
8	51	0.713 +/- 0.000	0.953 +/- 0.006
9	91	0.750 +/- 0.001	0.957 +/- 0.006
10	23	0.730 +/- 0.002	0.927 +/- 0.005
Mean		**0.726**	**0.957**

Figure Captions

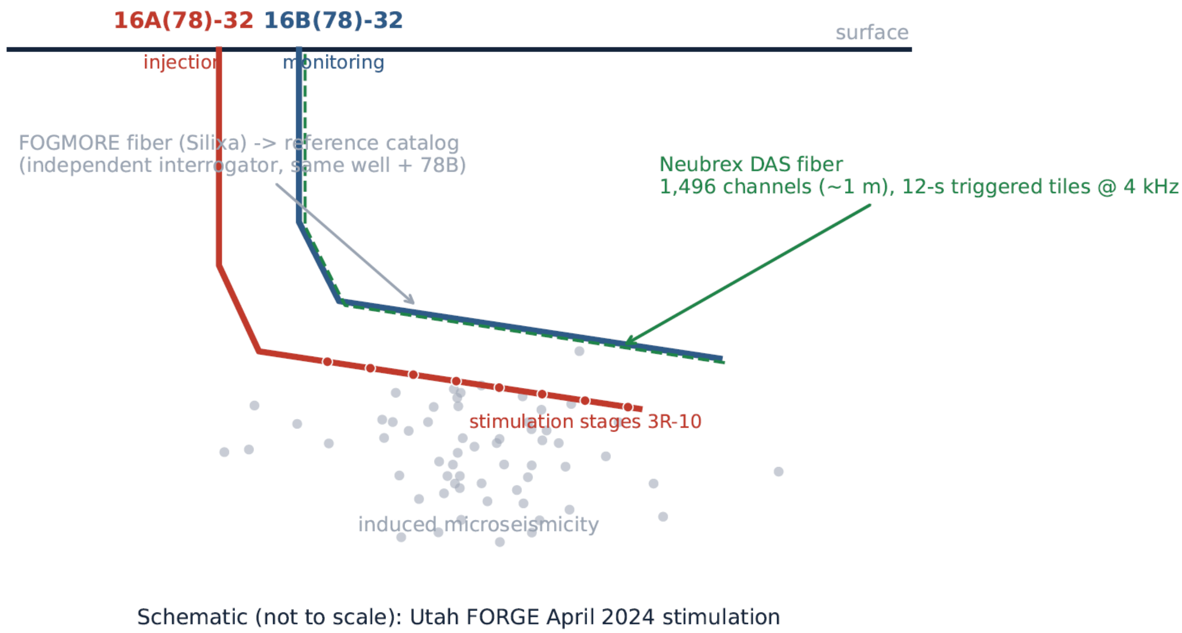

Figure 1. Schematic acquisition geometry (not to scale). The deviated injection well 16A(78)-32 (red) was stimulated in eight stages (3R and 4-10) in April 2024. The sub-parallel monitoring well 16B(78)-32 (blue) hosts the Neubrex single-mode fiber analyzed here (1,496 channels, 12-s triggered tiles at 4 kHz, green dashed) as well as the independent FOGMORE/Silixa fibers from which the reference catalog was derived together with vertical well 78B (gray).

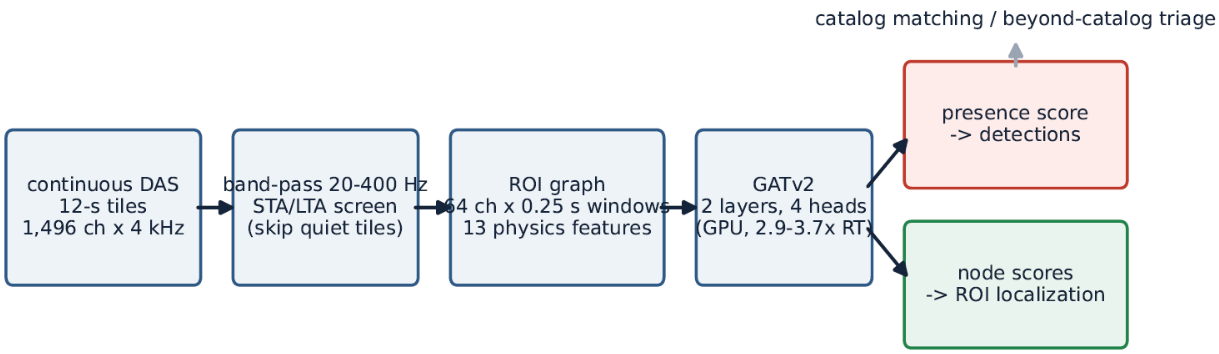

Figure 2. Processing pipeline. Continuous 12-s DAS tiles are band-pass filtered and screened by a cheap STA/LTA gate; surviving tiles are decomposed into overlapping 64-channel by 0.25-s regions of interest, each summarized by thirteen physical features and connected to its channel- and time-neighbors; a two-layer GATv2 outputs node scores (ROI localization) whose max-pool gives the tile presence score (detection). Measured throughput is 3.2-4.2 s per 12-s tile on one A100 GPU (2.9-3.7x real time).

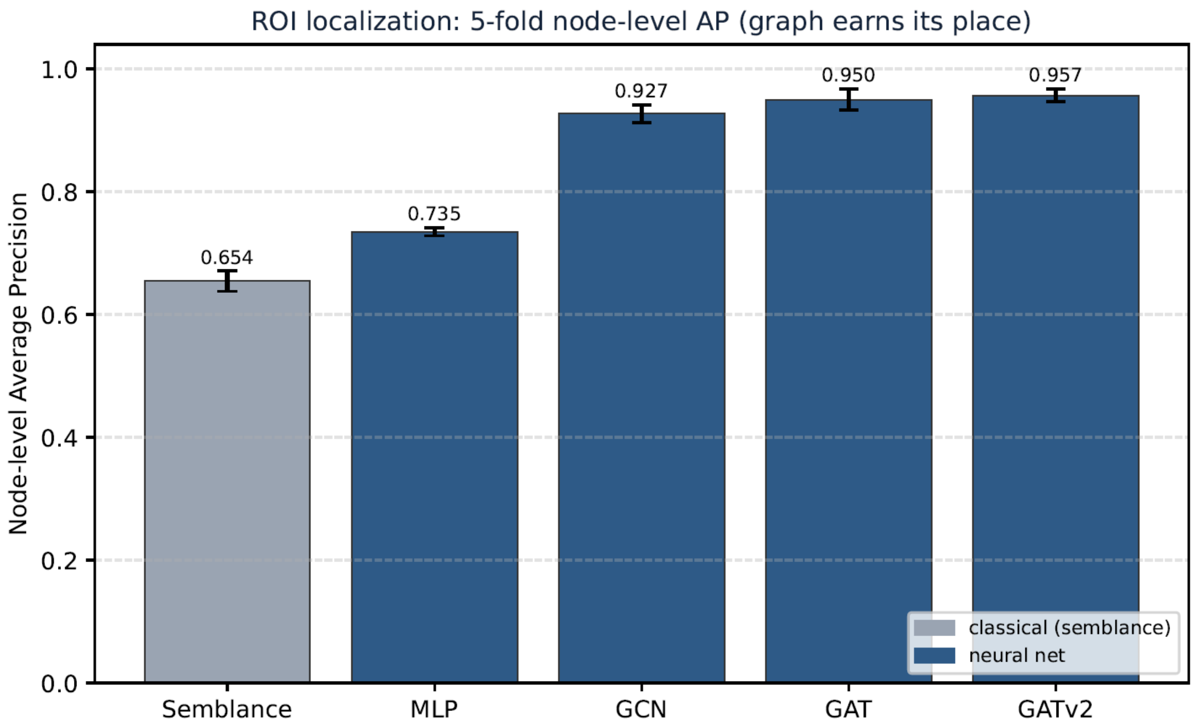

Figure 3. ROI localization requires the graph. Node-level average precision under leak-free 5-fold cross-validation for the classical semblance baseline and four learned architectures (mean +/- standard deviation across folds). Message passing (MLP to GCN) contributes the decisive gain; attention adds a further increment, with GATv2 best on average.

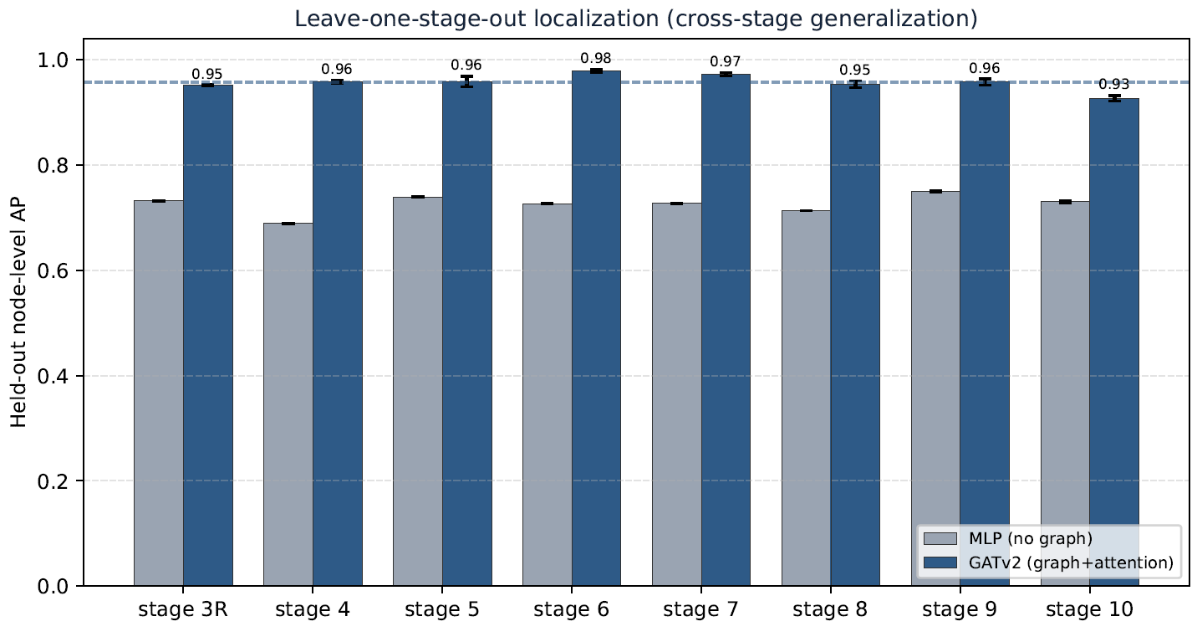

Figure 4. Leave-one-stage-out generalization. Held-out node-level average precision per stimulation stage (mean +/- standard deviation over three random seeds) for the no-graph MLP and GATv2; the dashed line marks the GATv2 mean (0.957). The graph advantage persists in every stage and the held-out mean equals the within-fold mean.

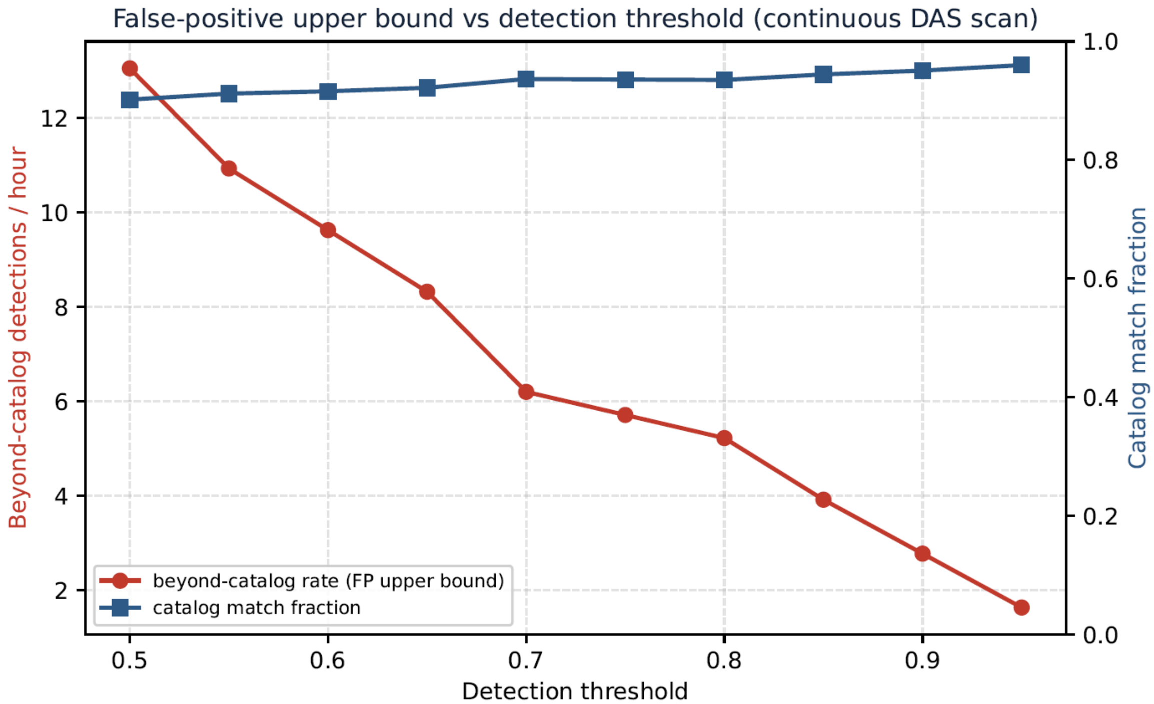

Figure 5. Operating-point trade-off of the continuous scan. Beyond-catalog detection rate (an upper bound on the false-positive rate, red) and catalog match fraction (blue) as functions of the detection threshold, computed over 6.13 hr of continuous stage-4 acquisition (815 detections at threshold 0.5).

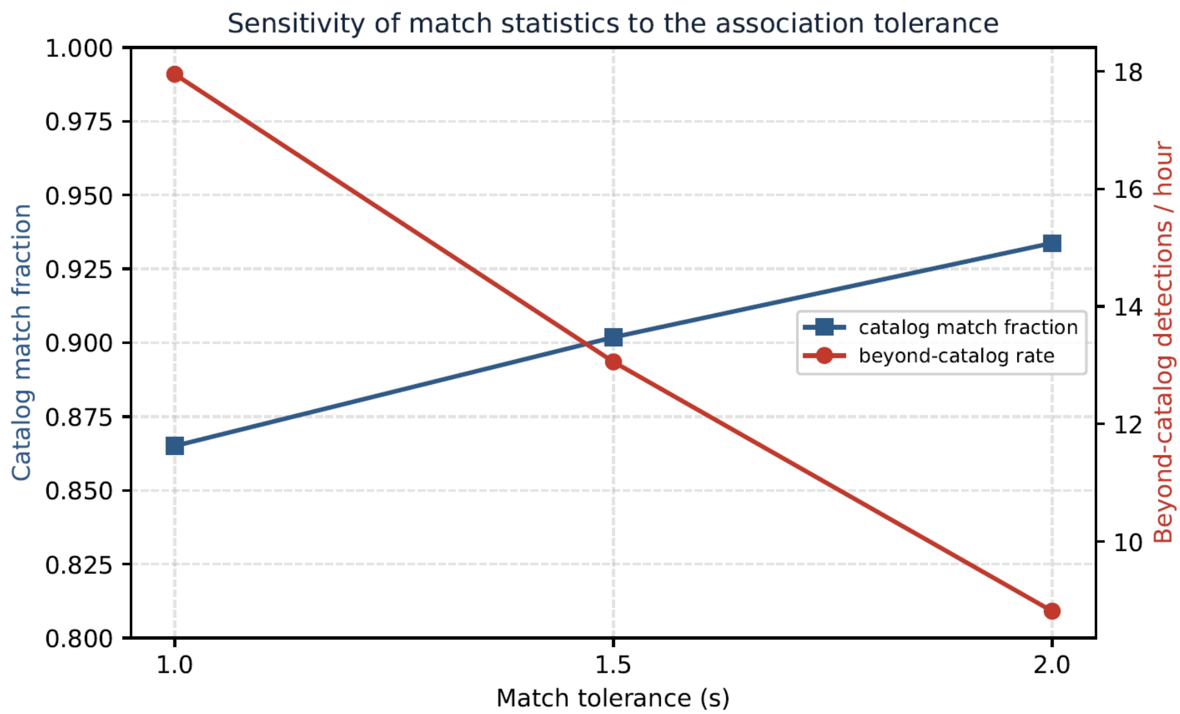

Figure 6. Sensitivity to the association tolerance. Catalog match fraction and beyond-catalog rate for tolerances of 1.0, 1.5, and 2.0 s; 54 beyond-catalog detections survive even the loosest window, so the beyond-catalog population is not a timing artifact.

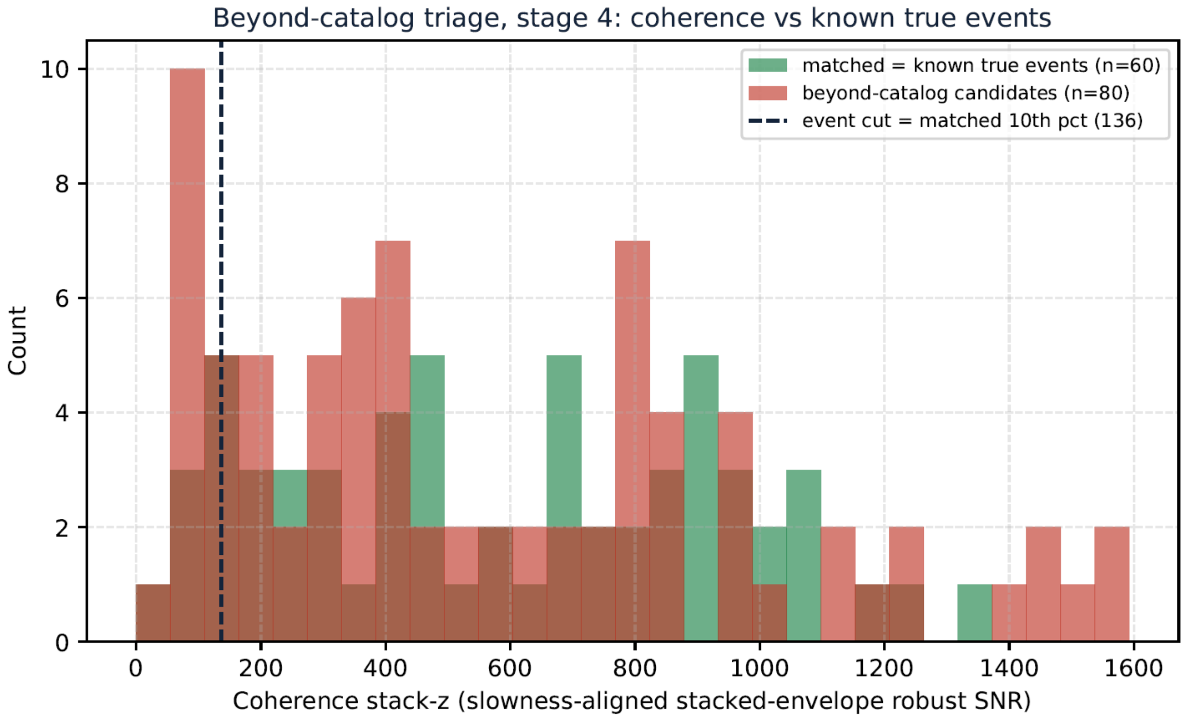

Figure 7. Coherence triage of beyond-catalog candidates (stage 4). Distribution of the stack-z coherence statistic for 60 catalog-matched detections (known true events, green) and the 80 beyond-catalog candidates (red); the event threshold (dashed) is the matched 10th percentile, so 90% of known events pass by construction. Sixty-five candidates (81%) exceed it; 26 also exhibit genuine (non-zero) moveout.

(a)

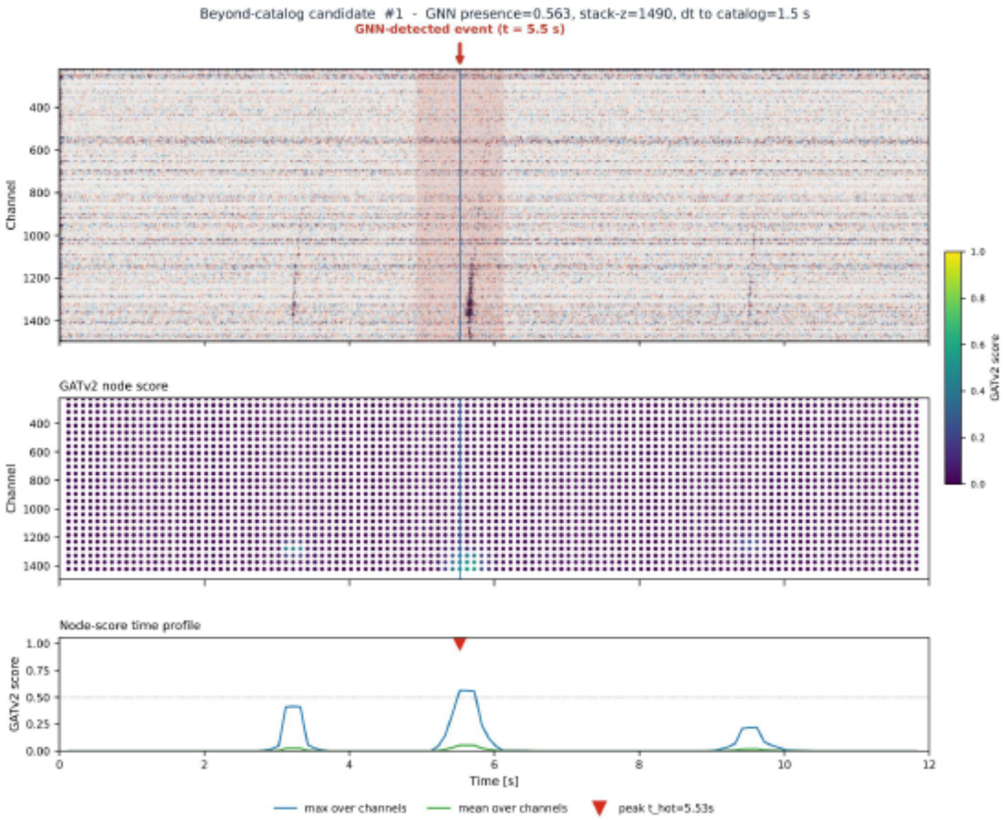

Beyond-catalog candidate #1 - GNN presence=0.563, stack-z=1490, dt to catalog=1.5 s
GNN-detected event (t = 5.5 s)
Channel
GATv2 node score
Channel
GATv2 score
Node-score time profile
GATv2 score
Time [s]
max over channels
mean over channels
peak t_hot=5.53s

(b)

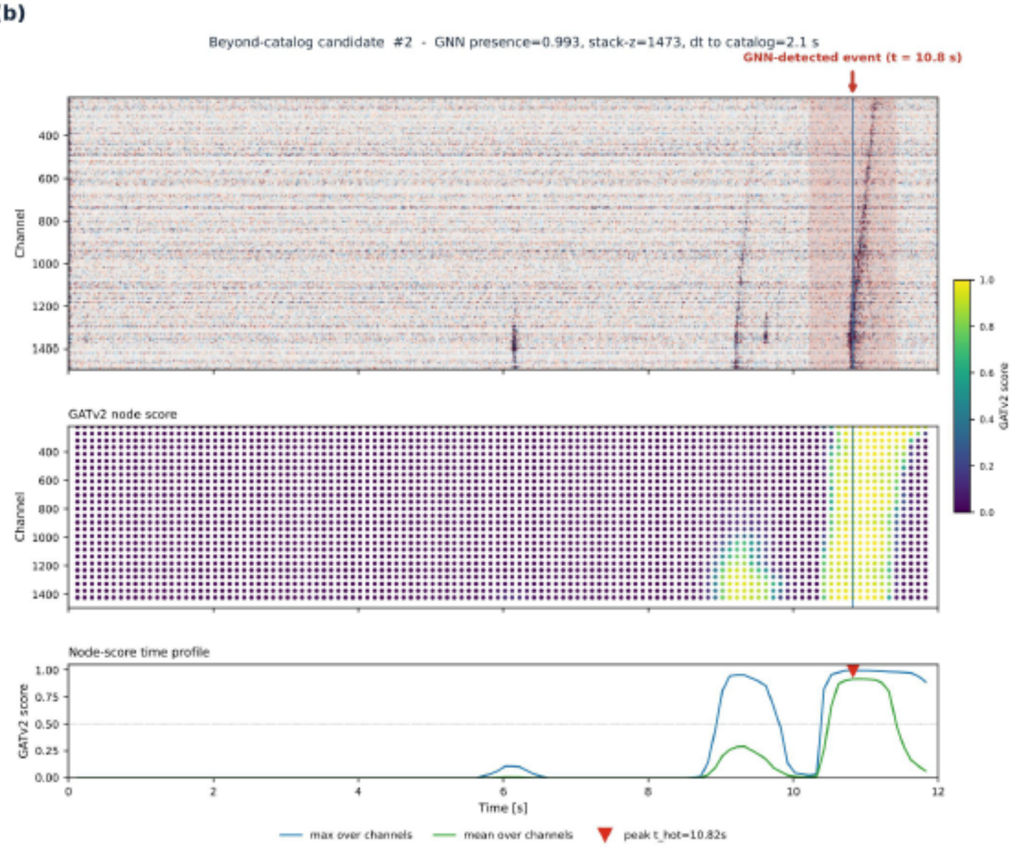

Beyond-catalog candidate #2 - GNN presence=0.993, stack-z=1473, dt to catalog=2.1 s
GNN-detected event (t = 10.8 s)
Channel
GATv2 node score
Channel
GATv2 score
Node-score time profile
GATv2 score
Time [s]
max over channels
mean over channels
peak t_hot=10.82s

Figure 8. Two representative beyond-catalog detections (stage 4), each showing the band-passed DAS waveform (top), per-ROI localization scores (middle), and the score time profile (bottom); the red marker and shaded window indicate the detection. Both events exhibit clear hyperbolic moveout at a common apparent slowness (-1.2 ms per channel) and are absent from the reference catalog. The full annotated gallery is provided in supplement S1.